

Multiphasic condensates formed with mono-component of tetrapeptides via phase separation

Received: 10 April 2024

Accepted: 12 March 2025

Published online: 19 March 2025

Check for updates

Laicheng Zhou^{1,2,3,6}, Longchen Zhu^{2,3,6}, Cong Wang^{4,6}, Tengyan Xu^{2,3},
Jing Wang^{2,3}, Bin Zhang⁴✉, Xin Zhang^{2,3,5}✉ & Huaimin Wang^{2,3,5}✉

Biomolecular condensates, formed by liquid-liquid phase separation of bio-macromolecules, play crucial roles in regulating physiological events in biological systems. While multiphasic condensates have been extensively studied, those derived from a single component of short peptides have not yet been reported. Here, we report the symmetrical core-shell structural biomolecular condensates formed with a programmable tetrapeptide library via phase separation. Our findings reveal that tryptophan is essential for core-shell structure formation due to its strongest homotypical π - π interaction, enabling us to modulate the structure of condensates from core-shell to homogeneous by altering the amino acid composition. Molecular dynamics simulation combined with cryogenic focused ion beam scanning electron microscopy and cryogenic electron microscopy show that the inner core of multiphasic tetrapeptide condensates is solid-like, consisting of ordered structures. The core is enveloped by a liquid-like shell, stabilizing the core structure. Furthermore, we demonstrate control over multiphasic condensate formation through intrinsic redox reactions or post-translational modifications, facilitating the rational design of synthetic multiphasic condensates for various applications on demand.

Cells evolve to form numerous membrane-enclosed organelles and membrane-less compartments to ensure complex cellular activities occur in a crowding environment. Membrane-less compartments enriched with proteins and nucleic acids, also named biomolecular condensates, are formed through liquid-liquid phase separation (LLPS)^{1–3}. Recent advances have unraveled intracellular multiphasic condensates represented by stress granules, nucleolus, and among others^{4–7}. The dynamic formation and dissociation of such sub-compartments inside condensates facilitate the regulation of complex cellular activities more precisely and spatiotemporally^{3,8,9}.

Biomolecular condensates are formed through the interplay of dynamic and multivalent weak noncovalent interactions, including electrostatic interactions, hydrophobic interactions, hydrogen bonds, π - π stacking, and cation- π interactions, among the intermolecular or intramolecular^{10–13}. Following the principles, several types of synthetic biomolecular condensates have been developed from IDP derivatives, polypeptides/RNA complex, and short peptide derivatives over the past few years^{14–21}. Recently, the synthesis of multiphasic condensates has attracted much attention, which often requires multi-components of proteins, peptides/RNAs complex, and polymers^{22–25}. To the best of

¹Department of Chemistry, Zhejiang University, Hangzhou 310058 Zhejiang Province, China. ²Department of Chemistry, School of Science, Westlake University, No. 600 Yungu Road, Hangzhou 310030 Zhejiang Province, China. ³Institute of Natural Sciences, Westlake Institute for Advanced Study, 18 Shilongshan Road, Hangzhou 310024 Zhejiang Province, China. ⁴Department of Chemistry, Massachusetts Institute of Technology, Cambridge, MA 02139, USA. ⁵Research Center for the Industries of the Future, Westlake University, No. 600 Dunyu Road, Sandun Town, Xihu District, Hangzhou 310030 Zhejiang Province, China. ⁶These authors contributed equally: Laicheng Zhou, Longchen Zhu, Cong Wang. ✉e-mail: binz@mit.edu; zhangxin@westlake.edu.cn; wanghuaimin@westlake.edu.cn

our knowledge, multiphasic condensates formed by a single component of short peptides have not been reported.

In this work, we describe the formation of mono-component tetrapeptide condensates with core-shell structures via phase separation by programming a tetrapeptide library (Fig. 1). Under the external pH/temperature stimuli, the single component of tetrapeptides could synchronously self-assemble into condensates with a core-shell structure. The outer shell of the condensates has better fluidity than the inner core. Mechanistic studies by Infrared spectroscopy (IR), Raman spectroscopy, and molecular engineering suggested that the hydrophobic interaction, π - π stacking, and hydrogen bonds contribute to the condensates formation of the tetrapeptide system. The amino acids mutation and atomic modification could modulate the homogeneity of condensates, indicating that tryptophan (W) is crucial for forming the core-shell structure. Molecular engineering combined with the MD simulation experiments showed that the stronger homotypical π - π interaction is the primary driving force for the assembly of core-shell condensates (Fig. 1a), resulting in the formation of ordered structures within the core, which was further stabilized by the liquid-like outer shell. Using molecular engineering to manipulate the balance of interactions between peptide-peptide and peptide-water, we can control the heterogeneity of condensates, either to be homogeneous or process core-shell structure (Fig. 1b). The transformation of the multiphasic condensates to be homogeneous could be easily controlled by an intrinsic redox reaction (Fig. 1c). Meanwhile, the distribution of the guest molecules can also be controlled

spatiotemporally (Fig. 1d). This work provides a general modular platform for constructing multiphasic condensates with a single component. What's more, the heterogeneity of tetrapeptide condensates could be modulated by tuning the strength of homotypical π - π interaction.

Results

Design and the formation of condensates through phase separation

The amino acid compositions of phase separation IDPs often involve the enriched polar residues, which are often scattered by aromatic residues^{26–30}. Tryptophan (W) rarely appears in IDPs and their contribution to phase separation is underappreciated. Associative polymers like proteins or polypeptides have higher valence than short peptides, enabling sufficient sticker-sticker interactions for phase separation^{29,31–33}. By contrast, short peptides with limited valence require more enthalpy or entropy compensation to drive phase separation at a low concentration. Increasing the strength of site-specific interactions among short peptides could promote phase separation. Among 20 amino acids, W has the largest hydrophobic and aromatic ring, providing the strongest π -system involved interactions and hydrophobic interactions, the NH group of the indole ring can further provide hydrogen bonds^{33,34}. Such strong interactions provided by W may lead to the collapse of proteins, which partially contributes to why W presents a limited ratio in the composition of both IDPs and low complexity regions (LCRs)³⁵. In contrast, involving W

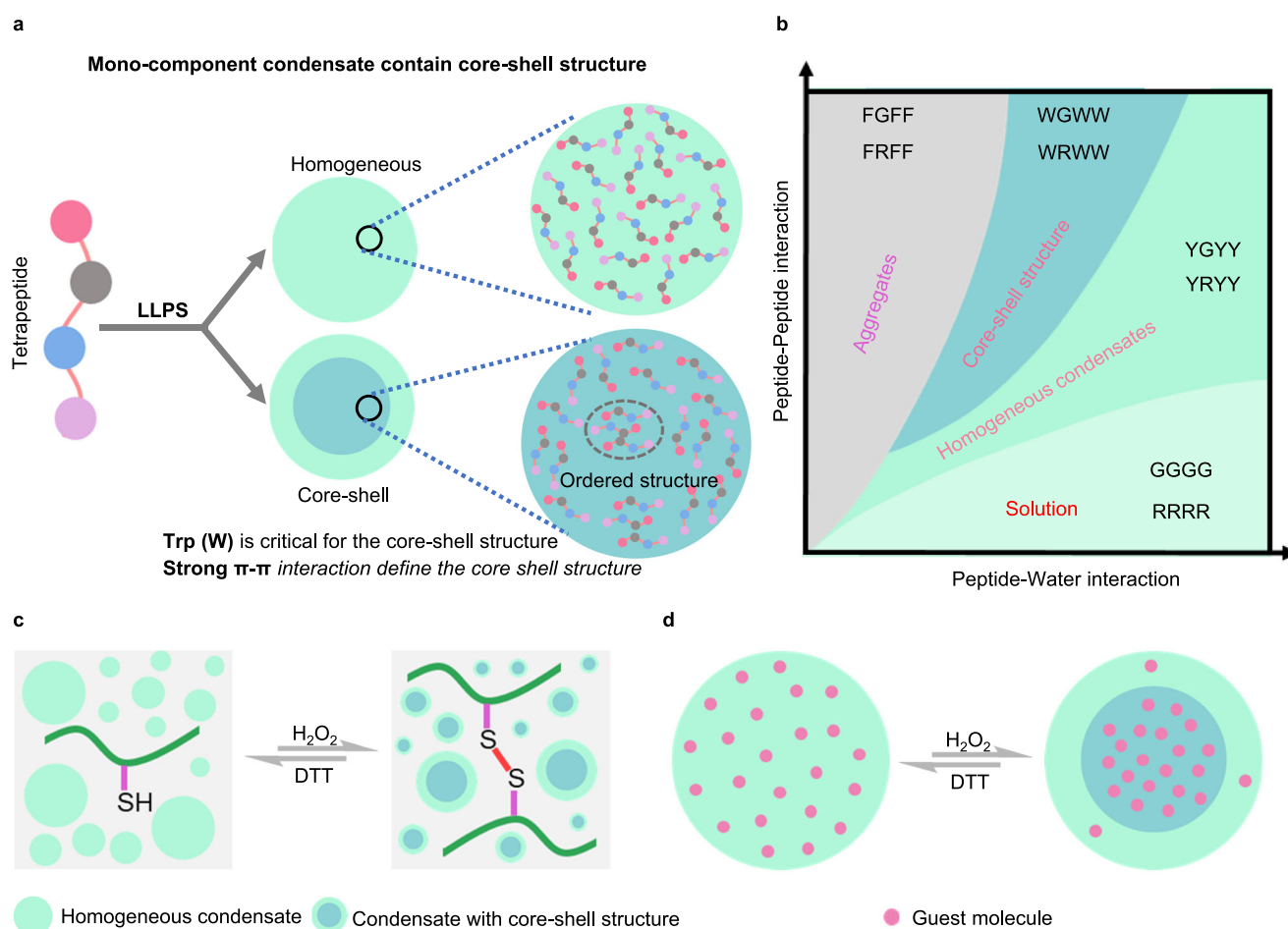


Fig. 1 | Biomolecular condensates with a core-shell structure formed by mono-component tetrapeptides. **a** Schematic illustration of the microstructure of condensates that can be tuned by amino acid composition. **b** Schematic illustration of the balance between peptide-peptide and peptide-water interactions that define

the phase separation behavior and structural properties of tetrapeptide condensates. **c** Schematic illustration of the redox-responsive condensates. **d** The homogeneously distributed guest molecules can be recruited into the newly formed inner core of condensates under the external stimuli.

seems to be the best choice to construct condensates composed of short peptides. Moreover, W exhibits distinctive and sharp Raman peaks, some of which have been demonstrated as a structural marker for the conformation, hydrogen bonding, hydrophobic interaction, and cation- π interaction, which could also facilitate our understanding of the molecular mechanisms for the formation of the liquid-liquid phase separation^{36–38}.

Inspired by the sticker-spacer model^{11,16,29,32}, we initially designed tetrapeptide WXXW (X is the guest residue, could be other 19 natural amino acids) and verified their capacity for phase separation. The C-terminus of the peptide is an amide group that can reduce its ability to self-assemble into hydrogels^{19,39}. Most WXXW peptides underwent phase separation and formed liquid-like condensates, but the concentrations of WXXW for phase separation are quite high (Fig. S2, Tab.S1). The saturation concentration significantly diminishes as the interaction valency increases^{11,40}, we substituted one of the spacer X by the Trp (W), which can provide higher or stronger valency than other amino acid residues and set another template-WXWW (Fig. 2a). Apart from 4 peptides (WVWW, WIWW, WDWV, and WEWW), the results showed that 16 peptides underwent phase separation and formed condensates with the external stimulus of pH (from acidic condition to neutral condition) or temperature (Fig. 2b, d, Fig. S3). The condensates formed by tetrapeptides with different residues exhibit different stability (Fig. 2c), one part of the condensates was relatively stable, and the other part could transform into aggregates within a few minutes or hours (Fig. S4). Besides pH and temperature, the phase separation of tetrapeptides was also exquisitely sensitive to different buffers (Fig. S5). The aggregation of condensates was possibly induced by the interaction between peptides and ions in the buffers⁴⁰. To comprehensively understand the properties of condensates and the interaction between peptides driving phase separation, we focused on the 6 stable condensates (WXWW, X = R, G, P, H, W, Y) and explored their phase separation behavior in double distilled water (dd H₂O), excluding disruption of the interaction between peptides and buffer components.

The phase separation of tetrapeptide could be induced by increasing pH at room temperature. We first measured the pH-dependent and temperature-dependent turbidity through absorbance at 600 nm. The results showed that the turbidity of the tetrapeptide solution increased dramatically when pH reached around 7.0 (Fig. 2e). The temperature-dependent turbidity demonstrates that the formed condensates all feature upper critical solution temperature (UCST) behaviors. The phase transition temperature of peptides increased as the hydrophobicity or aromaticity of the guest residues increased (Fig. 2f). The representative time-lapse images acquired from confocal laser scanning microscopy (CLSM) and Cryo-FIB-SEM images show the fusion of condensates, demonstrating its partial liquid-like property (Fig. S6, S17, supplementary movie 1). pH-concentration phase diagrams indicated that the tetrapeptides with the hydrophobic or aromatic guest residue (X = W, Y, P) need a lower pH/concentration to phase separate than the peptide WGWW (Fig. 2g). In contrast, the peptide with the hydrophilic amino acid (X = H, R) needs a higher pH/concentration to form condensates than the peptide WGWW (Fig. 2g). All the condensates shared similar pH and temperature reversibility, as demonstrated by the representative peptide WRWW through the measurement of its turbidity changes (Fig. 2h and Fig. 2i). These results demonstrated that tetrapeptides can form condensates with partial liquid-like properties with adaptation by tuning different guest residues.

The driving force for phase separation of tetrapeptide systems

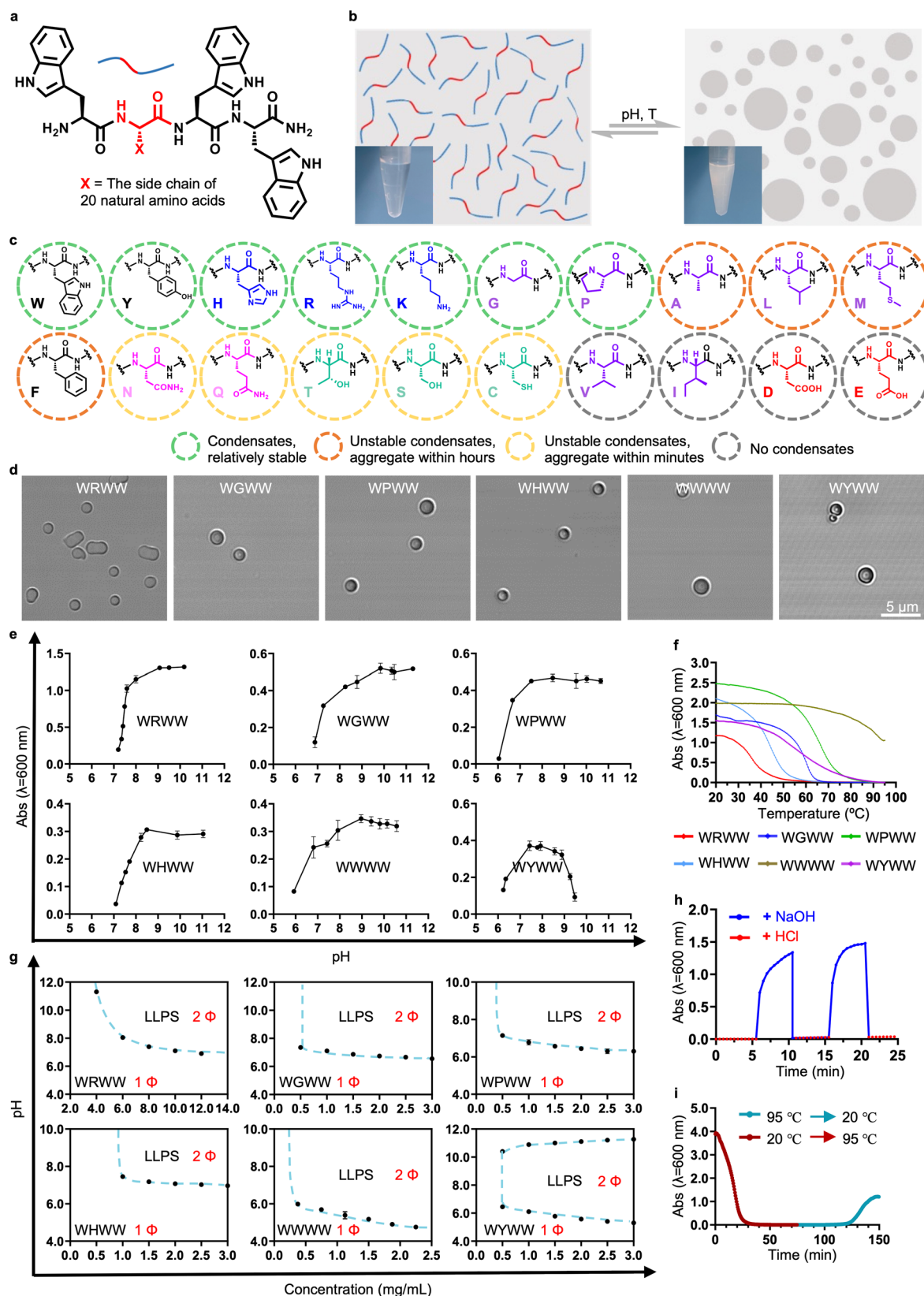
The condensation process could be induced by tuning pH to a neutral condition, indicating the phase separation may be triggered by the deprotonation of the amine group at the N-terminal. To verify the hypothesis, we compared the phase behavior of WGWW and Ac-WGWW-NH₂, in which the N-terminal is blocked by the acetyl group

(Fig. S7a). The phase separation behavior of Ac-WGWW-NH₂ is not affected by pH, while WGWW phase separates when pH approaches 7.0 (Fig. S7b, Fig. 2e, g), demonstrating the deprotonation of N-terminal amine groups is essential for triggering phase separation.

To further investigate the driving force that governs condensate formation, we used Fourier-transform infrared spectroscopy (FTIR) to shed light on the molecular interaction between peptides. For the control group of WRWW peptide solution, the peaks at 1672 cm⁻¹ (terminal amide) and the broad bands at 1656 cm⁻¹ (internal amide) in the FTIR spectrum indicate no order-organized intermolecular interactions of WRWW^{41–43} (Fig. 3a, blue curve). After the induction of phase separation, a significant peak appeared at 1645 cm⁻¹, suggesting the increased association of the amide groups between the backbone^{42,44,45} (Fig. 3a, red curve). The two peaks at 1608 cm⁻¹ and 1587 cm⁻¹ belong to the vibration of the aromatic ring shifted to 1603 cm⁻¹ and 1581 cm⁻¹, respectively, possibly due to the π - π stacking of the aromatic rings⁴⁴.

Next, we analyzed the side chain contribution of guest residues for phase separation by Raman spectroscopy (Fig. 3b, Fig. S8). The Raman peaks of residue Trp (W) can be used as markers to assign the different interactions that have been extensively reported^{36–38}: (i) hydrogen bond marker: 876 cm⁻¹ band, the indole ring vibration mode associated with a displacement of the N₁H group nearly along the N₁-H bond, which is very sensitive to hydrogen bonding and decreases with the strengthen of hydrogen bonding. (ii) van der Waals interaction marker: 1010 cm⁻¹ band, which is sensitive to the strength of van der Waals interactions of the indole ring with surrounding residues, the wavenumber increases with van der Waals interactions strengthen. (iii) hydrophobic interaction marker: 1340/1360 cm⁻¹ doublet. The larger intensity ratio $I_{(1360)}/I_{(1340)}$ indicates stronger hydrophobic interactions. (iv) cation- π interaction marker: the doublet centered at -755 and -764 cm⁻¹. The peak broadens and the intensity of the peak at -755 cm⁻¹ decreases and that at -764 cm⁻¹ increases when the Trp is involved in cation- π interactions³⁸. The peak around 877 cm⁻¹ means that the NH group on the indole ring is involved in a medium-hydrogen bond both in solution and condensate state (Fig. 3b, Fig. S8). For peptide WYWW, the intensity ratio of the doublet at 850 cm⁻¹ and 830 cm⁻¹ is about 1.3 (Fig. S9a), indicating moderate hydrogen bonding by the hydroxyl group of tyrosine^{46,47}. The measured Raman shift of 1010 cm⁻¹ suggests weak Van der Waals interactions in solution and condensate states (Fig. S8). The values of the intensity ratio $I_{(1360)}/I_{(1340)}$ dramatically increased when the condensates formed, indicating stronger hydrophobicity within the condensates than in the solution state^{36,37} (Fig. 3c, Fig. S9b). The cation- π interaction, especially between Arg (R) and Trp (W) usually plays a crucial role in driving LLPS^{11,13,18}. However, from the spectra of WRWW, no significant changes were observed near the doublet centered at -755 and -764 cm⁻¹, indicating no obvious cation- π interactions involved with the Trp³⁸ (Fig. 3d). The capacity of WGWW, which lacks side chain, to form stable condensates further supports this possibility. In addition, we also excluded the possible cation- π interaction through the N-terminal amine cation by acetyl group block, the peptide Ac-WGWW-NH₂ can still form condensates (Fig. S7b). Finally, we excluded the possible cation- π interactions between Na⁺ and Trp (W) by using the organic base triethylamine (TEA) instead of the sodium hydroxide solution to adjust the pH, all these peptides can still undergo phase separation (Fig. S10). All these results indicate that the cation- π interactions are unnecessary for the phase separation of tetrapeptide systems.

The above results suggested that the increased hydrophobic interaction, π - π stacking, and the hydrogen bonds drive the phase separation of the tetrapeptides cooperatively. To further verify this conclusion and expand the tetrapeptide library, we next synthesized the peptides FRFF and YRYY, due to Try (Y) and Phe (F) having aromatic rings similar to Trp (W) among other natural amino acids to provide enthalpy compensation. The results showed that FRFF formed aggregates while YRYY formed liquid-like condensates, indicating that

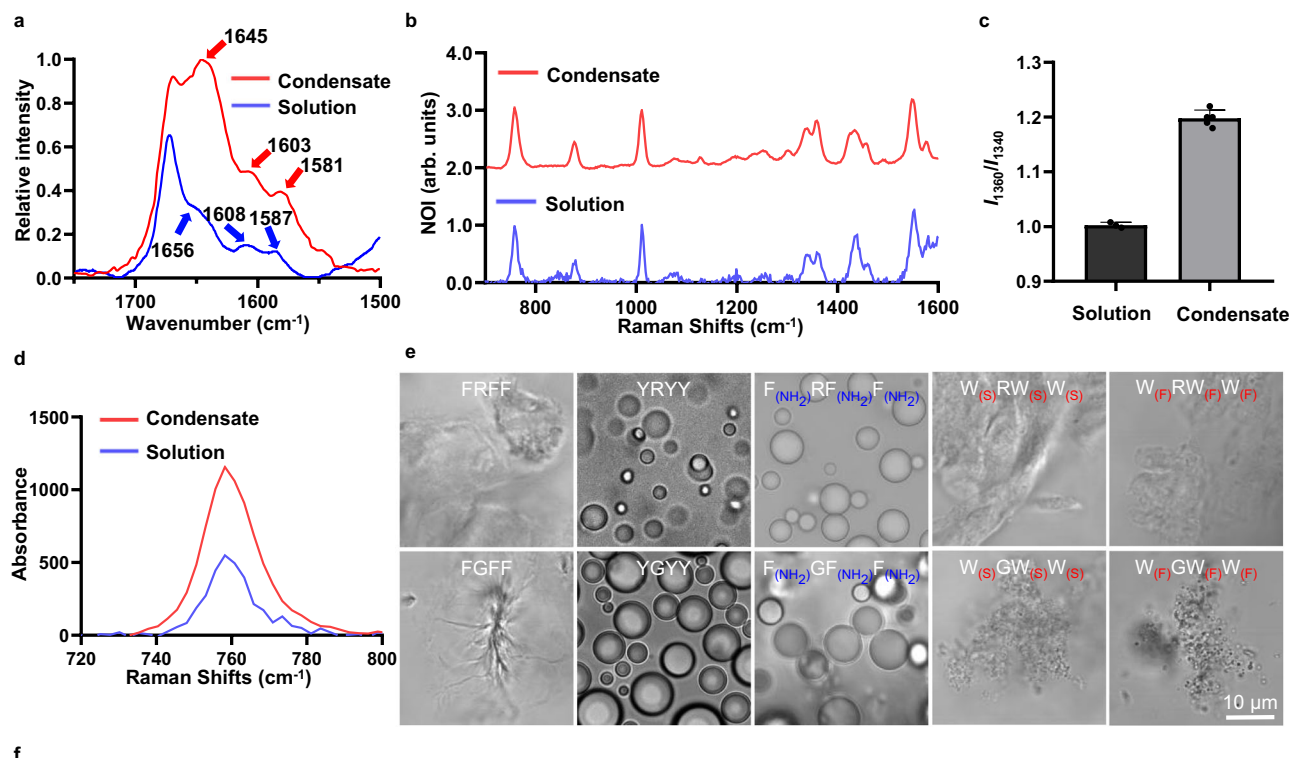


the hydrophilic group on the aromatic ring is important to maintain the condensate states for tetrapeptide (Fig. 3e, f). To verify the contribution of hydrophilic groups on the aromatic ring, we synthesized peptide, $F_{(NH_2)}RF_{(NH_2)}F_{(NH_2)}$, with amine groups that can provide extra hydrogen bonds and facilitate the solvation of the aromatic ring. We also synthesized the peptide $W_{(S)}RW_{(S)}W_{(S)}$, the NH group on the

indole ring was substituted by sulfur (S), which could decrease the strength of hydrogen bonds and solvation of the peptide. As a result, $F_{(NH_2)}RF_{(NH_2)}F_{(NH_2)}$ formed liquid-like condensates as the peptide $W_{(S)}RW_{(S)}W_{(S)}$ formed aggregates, demonstrating that the hydrogen bonding sites on the aromatic ring are essential for the formation of the condensates. Moreover, the fluorine substituted peptide

Fig. 2 | Phase separation of tetrapeptides. **a** Chemical structure of tetrapeptide WXWW. **b** Schematic illustration for phase separation of tetrapeptide WXWW. **c** The summary of phase separation behavior of WXWW. **d** Bright-field images of condensates formed by tetrapeptides WXWW with different guest residues R/G/P/H/W/Y (double distilled water, pH 7.5 ± 0.5). **e** The pH-dependent turbidity changes of peptide WXWW with different guest residues R/G/P/H/W/Y solution that is measured by spectrophotometer at the absorbance of 600 nm. Data are presented

as mean values ± SD, $n = 3$. **f** Upper critical solution temperature of peptides WXWW with different guest residues R/G/P/H/W/Y that measured by spectrophotometer (double distilled water, pH 7.5 ± 0.5). **g** pH-concentration phase diagrams of peptides WXWW with different guest residues R/G/P/H/W/Y in an aqueous solution at room temperature. Data are presented as mean values ± SD, $n = 3$. **h** pH, and **i** temperature reversibility curve of WRWW (12 mg/mL, double distilled water, pH 7.5 ± 0.5). Source data are provided as a Source Data file.



f

<p>F Y F(NH₂)</p>	FRFF	YRYY	F(NH ₂)RF(NH ₂)F(NH ₂)
	FGFF	YGY	F(NH ₂)GF(NH ₂)F(NH ₂)
	Aggregates	Condensates	Condensates
Control	(+) Solvation of the aromatic ring	(+) Solvation of the aromatic ring	
	(+) Hydrogen bond	(+) Hydrogen bond	
<p>W W(S) W(F)</p>	WRWW	W(S)RW(S)W(S)	W(F)RW(F)W(F)
	WGWW	W(S)GW(S)W(S)	W(F)GW(F)W(F)
	Condensates	Aggregates	Aggregates
Control	(-) Solvation of the aromatic ring	(-) Solvation of the aromatic ring	
	(-) Hydrogen bond	(-) π-π stacking	
		(+) Dipole-Dipole interaction	

Fig. 3 | The mechanism underlying liquid-liquid phase separation. **a** The IR spectra of WRWW in solution and condensates state (12 mg/mL, pH 7.5 ± 0.5). **b** The Raman spectra of WRWW in solution and condensates state (12 mg/mL, pH 7.5 ± 0.5), NOI (Normalized offset intensity). **c** Hydrophobic interaction in solution and condensate state of WRWW measured by I_{1360}/I_{1340} . Data are presented as

mean values ± SD, (solution, $n = 3$; condensate, $n = 5$). **d** The partially enlarged Raman spectra of WRWW in solution and condensates state. **e** The bright field images of the microstructure formed by different tetrapeptides. **f** The relationship between the chemical structure and their microstructure. Source data are provided as a Source Data file.

W(F)RW(F)W(F) also forms the aggregates, possibly because the π-π stacking of the aromatic rings was disrupted by the increased dipole-dipole interaction or the decreased solvation of the aromatic ring^{48,49}. In parallel, we also synthesized the peptides YGY, FGFF,

W(S)GW(S)W(S), F(NH₂)GF(NH₂)F(NH₂), W(F)GW(F)W(F). X = G share the similar phase behavior with parallel group of X = R (Fig. 3e), further demonstrating the great contribution of hydrophilic groups on the aromatic ring for phase separation.

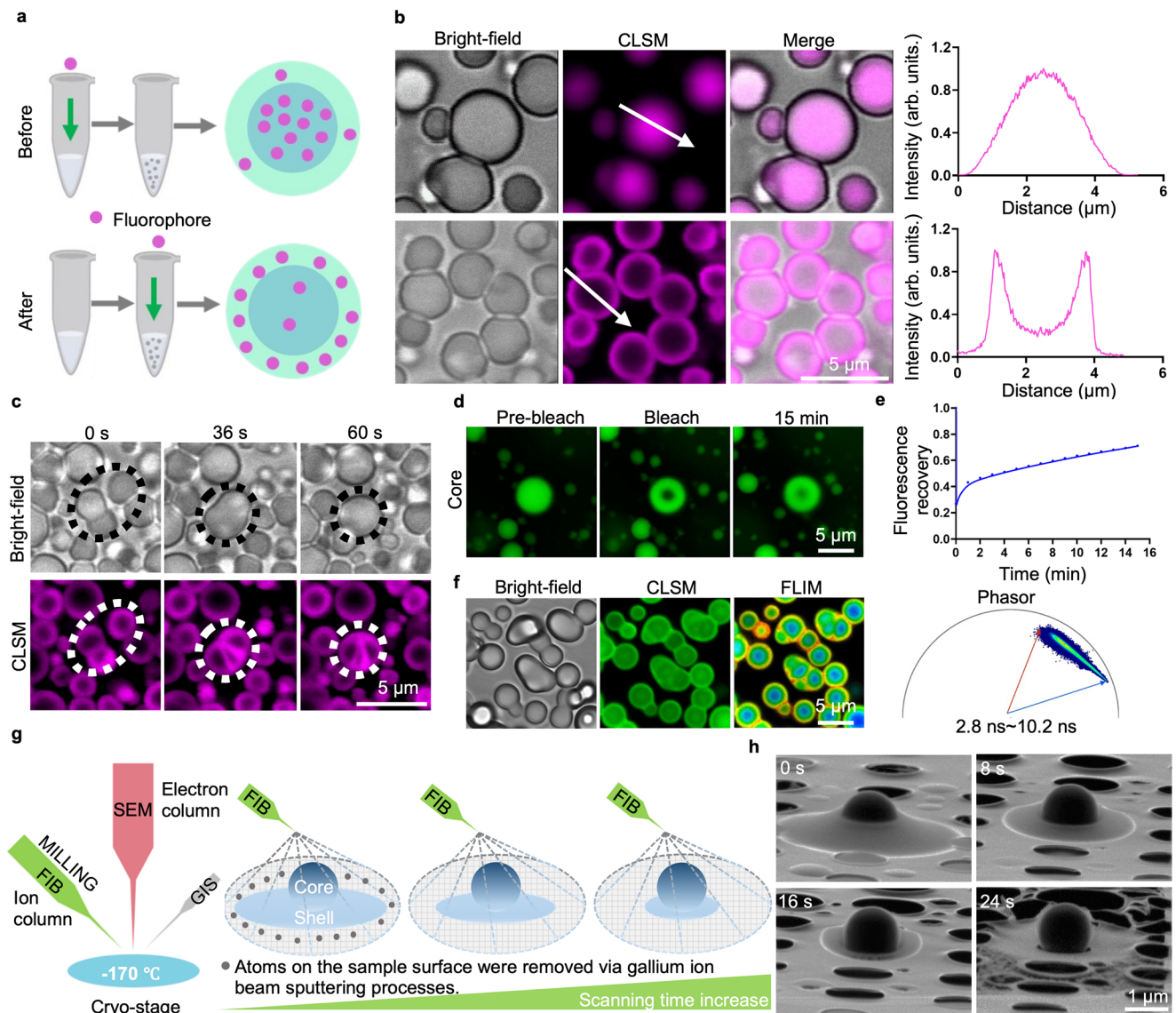


Fig. 4 | The core-shell structure of the condensates formed by WRWW.

a Schematic illustration of the fluorophores added before and after the condensate formation. **b** The CLSM images of the rhodamine B added before and after the condensate formation (WRWW, 18 mg/mL, pH 7.5 ± 0.5). **c** Time-dependent CLSM images show the changes of the inner core during the fusion process of the outer shell (WRWW, 18 mg/mL, pH 7.5 ± 0.5). **d**, **e** Fluorescence recovery after

photobleaching (FRAP) experiment, free fluorescein (1 μ M). **f** DIC, CLSM, FLIM, and Phasor images of the condensates after adding SBD. **g** Schematic illustration of the Cryo-FIB/SEM hardware component and the changes of the condensates under the gallium ion beam sputtering. **h** Time-dependent Cryo-FIB-SEM images of the condensates under the gallium ion beam sputtering (WRWW, 12 mg/mL, pH 9.0 ± 0.5). Source data are provided as a Source Data file.

Above all, the interactions among peptide-peptide and peptide-water contribute to the LLPS synergistically. The peptide-water interaction plays a dominant role in the acidic solution state, which leads to better dissolution. With the pH increase, the amine group of the N-terminal began to deprotonate which caused the hydrophobicity of the peptide to increase, following the clustering of the peptide. The increased association of the backbones and side chains work cooperatively to stabilize the condensates. The aromatic rings without the hydrophilic group could hardly interact with the aqueous solvent, the peptide-peptide interaction could not be balanced by peptide-water interaction, resulting in the formation of aggregates rather than condensates. Other factors that disrupt the π - π stacking or increase the hydrophobicity could also cause the formation of the aggregates (Fig. 3f).

The tetrapeptide condensates with a core-shell structure

Biomolecular condensates show the capacity for concentrating biomolecules to facilitate biocatalysis⁵⁰. Three peptides (WGWW, WYWW,

WRWW), which stand for peptides with no side chain, hydrophobic side chain, and hydrophilic side chains were systematically investigated, and the results of representative peptide WRWW are shown in Fig. 4. We first measured the ability of tetrapeptide condensates to recruit guest molecules from surrounding milieu. We selected fluorophores (fluorophores including coumarin 6, SBD, rhodamine 6 G, rhodamine B, and BODIPY) to quantify the encapsulation efficiency by fluorescence spectroscopy of the supernatant, which is obtained by centrifugation of condensate solution (Fig. S11). The partition efficiencies of six fluorophores into WGWW, WYWW, and WRWW condensates are all remarkably high, averaging around 90% (Fig. S12).

Intriguingly, further observation by CLSM revealed that the fluorescent dye has different distributions within the WRWW condensates when added before or after the condensate formation (Fig. 4a). When the addition of fluorophore was before the condensate formation, the fluorescent molecules were mainly located at the inner core of the condensates (Fig. 4b top panel). Meanwhile, with the

addition of fluorophore after the condensate formation, we found the condensates exhibit a vesicular-like structure (Fig. 4b bottom panel, Fig. S13). These results together implied that the condensates could have a core-shell structure, which could spatially control the distribution of guest molecules (Fig. S14).

Since the bright-field images could not recognize the core-shell structure, we tried to use CLSM to visualize the fusion process of multiphasic condensates. The time-lapse images (supplementary movie 2) show that the inner core of the condensates has been squeezed to deform rather than fuse during the fusion processes of the outer shell, suggesting that the inner cores are more solid-like than outer shell (Fig. 4c). We next performed the fluorescence recovery after the photobleaching (FRAP) experiment at the center of condensates. The fluorescence recovery rate of the inner core is quite slow, suggesting that fluorescent molecules experience strong molecular interaction within the inner core (Fig. 4d, e). To investigate the difference in the microenvironment of the core and shell of the condensates, we used fluorescence lifetime imaging microscope (FLIM) experiments by using sulfonamide benzoxadiazole (SBD), which is a polarity-sensitive dye that could report the average microenvironmental polarity close to the fluorophores by exhibiting distinctive fluorescence lifetimes²⁵. The results show that the lifetime of SBD gradually decreases from the outer shell to the inner core, demonstrating that the condensates are inhomogeneous (Fig. 4f, supplementary movie 3). To exclude the possible interpretation of lifetime caused by the indole ring from the Trp, or the trapped water of the inner core, we used the Cryo-EM, Cryo-FIB-SEM to observe the core-shell structure directly. The results show that the spherical core is surrounded by the collapsed outer shell (Fig. S15). The time-dependent Cryo-FIB-SEM images indicate that the outer part of condensates quickly disappeared because the atom of the sample can be continuously removed via the ion beam sputtering process. Meanwhile, the inner core is relatively stable when simultaneously exposed to the same gallium ion beam (Fig. 4g, h, Figs. S16, S17). This result indicates that the molecules are packed more tightly or interact more strongly in the inner core than in the outer shell.

The strong homotypical π - π interaction defines the core-shell structure

The complex architecture of tetrapeptide condensates shows the potential for developing different functions within the core and shell. Understanding the driving force and underlying mechanism for the formation of multiphasic condensates may facilitate the design and development of synthetic organelles^{51,52}. We first investigated the main driving force to determine the core-shell structure by comparing the condensates with different amino acid compositions. As a very slight change in the crosslinks at the molecular level can dramatically strengthen or weaken the percolation or self-association of the condensed phase^{32,33,54}. We substituted the Trp (W) residues in the sequence WRWW with Tyr (Y), and the resulting peptides YRYY formed homogeneous condensates rather than core-shell structure (Fig. 5a, b), implying the stronger homotypical interaction between Trp (W) may account for the core-shell condensate formation.

To verify our hypothesis and figure out what kinds of driving forces determine the core-shell structure, we synthesized the peptide $W_{(OH)}RW_{(OH)}W_{(OH)}$ and $W_{(DHT)}RW_{(DHT)}W_{(DHT)}$ (Fig. 5a). The peptide $W_{(OH)}RW_{(OH)}W_{(OH)}$ increased 3 hydrogen bonding sites on each molecule compared with the peptide WRWW, which does not substantially affect the core-shell structure (Fig. 5b left panel). We aborted the double bond on the indole ring to form $W_{(DHT)}RW_{(DHT)}W_{(DHT)}$, which is no longer conjugate to the benzene ring, thus reducing the aromatic interaction compared with WRWW. The CLSM and fast FLIM results all show that $W_{(DHT)}RW_{(DHT)}W_{(DHT)}$ forms homogeneous condensates (Fig. 5b middle panel), indicating stronger homotypical π - π interaction is essential for the multiphasic condensate formation. Similarly, the

amino acid Tyr (Y) has a smaller aromatic ring than Trp (W) residue, the smaller homotypical π - π interactions could weaken the crosslink of molecules within the condensed phase during phase separation, resulting in the formation of homogeneous condensates (Fig. 5b right panel). Moreover, the parallel group $WGWW$, $W_{(OH)}GW_{(OH)}W_{(OH)}$, $W_{(DHT)}GW_{(DHT)}W_{(DHT)}$, YGYG show similar results with the R group (Fig. S18). These results suggested that the strong homotypical π - π interaction is the main driving force for the formation of core-shell structural condensates.

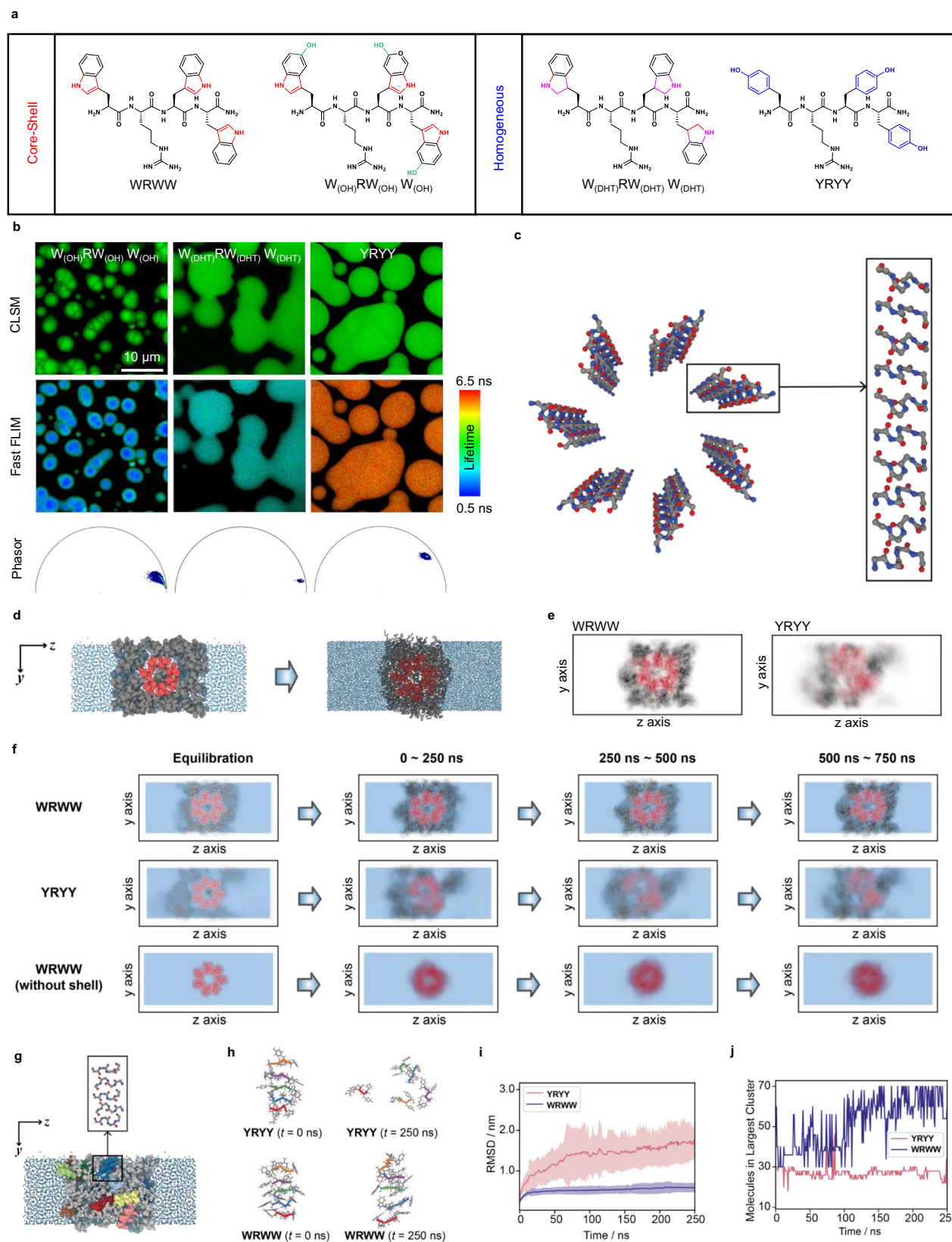
Subsequently, we further explored the mechanism behind the formation of the condensed inner cores. Tetrapeptide usually tends to self-assemble into hydrogels or fibers rather than liquid-liquid phase separation⁵⁵, and aromatic-aromatic interactions are beneficial to the formation of fibers or beta-sheet structures⁵⁶. The LLPS peptides in our system still reserve the propensity of self-assembly, which increases with increasing pH. Moreover, the sequences which form core-shell condensates has stronger self-assembly ability than the sequences that form homogeneous condensates at the same condition (Fig. S19). We hypothesized that the solid-like core may form or be stabilized by some self-assembled ordered structures, such as fibers or fiber-like clusters, which was then demonstrated by cryo-EM results (Fig. S20). The cross-section of the inner core was acquired by cryo-FIB milling, the following cryo-EM observation demonstrated the existence of ordered structures.

To further support our hypothesis, a multiscale MD simulation approach was adopted to efficiently and accurately simulate tetrapeptide systems. Two sets of simulations were conducted to study the stability of the core-shell structures for various WXWW systems and their formation process.

For simulations that evaluate the stability of the core-shell structures, we constructed the initial configurations with an ordered structure forming the condensate core, surrounded by a liquid-like shell composed of tetrapeptide monomers (Fig. 5d, Fig. S21). The solid-like core structure (Fig. 5c) is adapted from the I-KME₃ fiber (PDB ID: 6X5I)⁵⁷, which is a fiber formed by short peptides and has been well characterized using CryoEM. We initialized the simulation box with an ordered core surrounded by tetrapeptide monomers in a slab simulation box. We simulated both acidic and basic environments for the WRWW and YRYY systems, resulting in four distinct simulations. Each simulation started with a 1 μ s long coarse-grained simulation using the MARTINI 3 model⁵⁸, followed by a more detailed 750 ns all-atom simulation using the CHARMM36m force field⁵⁹. To analyze phase separation behavior and stability of the ordered core in WRWW and YRYY systems, we computed the average probability density of various molecules across the yz-plane throughout the all-atom simulation process.

The simulation results agreed with experimental observations. In an acidic environment, both WRWW and YRYY systems transitioned to a single, homogeneous dilute phase, with the condensed phase absent (Figs. S22, S24). In contrast, the condensed phase persisted in both systems in a basic environment (Fig. 5e, Figs. S22, S23). Notably, in a basic environment, the ordered core maintained its original structure in the WRWW condensed phase, while the core dissipated in the YRYY condensate (Fig. 5e). This observation aligns with experimental results, which show that the solid core exists in WRWW systems but not in YRYY systems under basic conditions. The consistency between simulations and experimental findings supports the formation of a core with an ordered structure within the WRWW condensate. Additional simulations conducted on WGWW and YGYG yielded analogous results, which are reported in the Supplementary Information (Figs. S22, S23, and S24).

In addition to simulations of the solid-like core within a liquid shell, we conducted a simulation for a bare WRWW core without a surrounding liquid shell to investigate the rationale behind the formation of the core-shell microstructure. Comparison of the density



distributions of the WRWW core during the simulation, both with and without the liquid shell, revealed that the absence of a liquid shell allowed more solvent water to penetrate between peptides, leading to the gradual dissolution of the ordered core structure (Fig. 5f). This observation provides insight into the existence of the core-shell structure in WRWW condensates: water molecules, interacting at the

exterior of the condensed phase, exert a significant influence on peptide-peptide interactions. These interactions disrupt the ordered core structure, inducing a transition towards a disordered liquid state at the exterior of the condensed phase. The equilibrium between peptide-peptide and peptide-water interactions results in a disordered liquid-like shell encapsulating the ordered solid-like core.

Fig. 5 | The mechanism underlying the formation of the core-shell structure.

a Chemical structure of the peptides WRWW, $W_{(OH)}RW_{(OH)}W_{(OH)}$, $W_{(DHT)}RW_{(DHT)}W_{(DHT)}$, YRYY. **b** The confocal and fast FLIM images of the peptides $W_{(OH)}RW_{(OH)}W_{(OH)}$, $W_{(DHT)}RW_{(DHT)}W_{(DHT)}$, YRYY with fluorophore SBD. **c** Backbone structure of the ordered core used for MD simulations, adapted from the configuration of 1-KMe₃ fiber⁵⁷. **d** Multiscale simulation scheme. The initial structure of the all-atom simulation (right) was prepared using the MARTINI simulation (left). The color coding is consistent across panels d, e, and f: core peptides (red), shell peptides (black), and water (blue). **e** Average peptide density profile for the last 250 ns of the simulation in a basic environment. **f** Average density profile of WRWW, YRYY,

and WRWW (without shell) across different simulation time windows. **g** Initial configuration used in simulations to probe the formation process of core-shell structures. These simulations include 14 replicas of beta-strands, each represented in distinct colors, embedded within a condensate composed of individual tetrapeptides, which are depicted in gray. **h** Representative beta-strand structures for WRWW and YRYY before and after simulation. **i** Mean RMSD of beta-strands as the simulation progresses, with shaded areas indicating the standard deviation of RMSD calculated from 14 replicas. **j** Number of peptides in the largest clusters for WRWW and YRYY along the simulation. Source data are provided as a Source Data file.

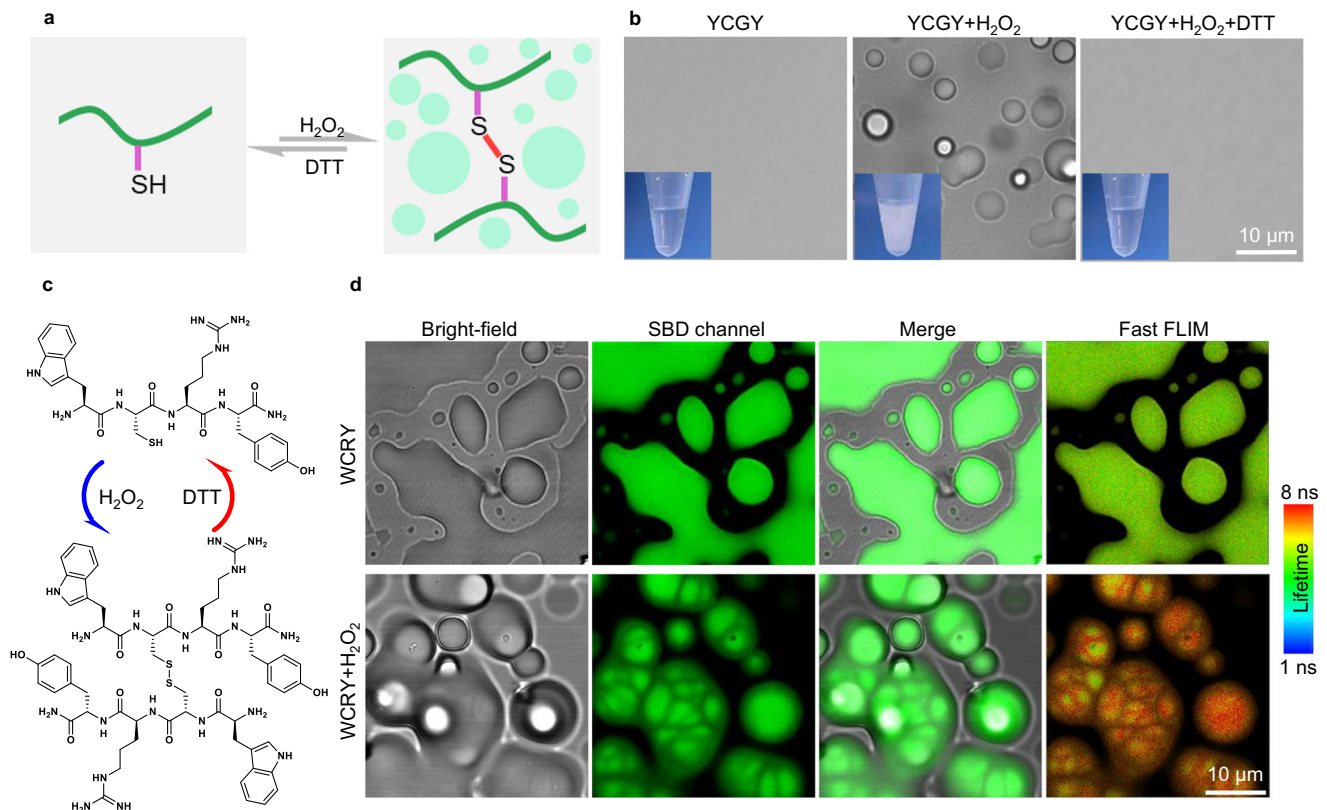


Fig. 6 | The dynamic and reversible control of LLPS and core-shell structure of the condensates. **a** Schematic illustration of redox reaction control phase separation of tetrapeptide. **b** Bright-field images of the peptide solution, oxidized and cross-linked by H_2O_2 , then reduced by DTT. **c** The cross-linking and

dissociation of peptides during the transformation between core-shell and homogeneous condensates. **d** Confocal and fast FLIM images of the homogeneous condensates and the core-shell structure of the condensates formed by the oxidation of H_2O_2 .

Another set of MD simulations was performed to investigate the formation process of core-shell structures. Directly simulating this process is currently infeasible due to the need for atomistic simulations over prohibitively long timescales, rendering it computationally impractical. Instead, we focused on two critical steps that provide evidence for the formation of core structures: (1) the stabilization of beta strands by tetrapeptides and (2) the aggregation of these beta strands into core structures. These simulations began with 14 beta strands, each consisting of five tetrapeptides, randomly distributed in a condensed solution containing 130 tetrapeptides (Fig. 5g). Simulations were conducted for both WRWW and YRYY sequences under basic conditions. The systems were first equilibrated using MARTINI simulations, followed by 250 ns of atomistic simulations.

To evaluate the stability of beta strands, the root mean square deviation (RMSD) of strand configurations over time relative to their initial structures was calculated. WRWW exhibited significantly lower RMSD values compared to YRYY (Fig. 5h, i), indicating greater stability of beta strands in WRWW. This finding supports the hypothesis that WRWW promotes the formation of beta strands, which are critical for

assembling core structures. Beta strand aggregation was further analyzed using DBSCAN clustering⁶⁰ to track the number of peptides in the largest clusters over time. For WRWW, nearly all beta strands aggregated into a single, large cluster, whereas YRYY formed smaller and more fragmented clusters (Fig. 5j). These results demonstrate that WRWW not only stabilizes beta strands more effectively but also exhibits a stronger propensity for aggregation, both of which are key steps in fiber and core-shell structure formation.

Dynamic control phase separation process and transformation between multiphase and homogeneous condensates

We have shown that the absence of a hydrophilic group in the aromatic ring often causes the tetrapeptides unable to form stable condensates caused by unbalanced strong peptide-peptide interaction and peptide-water interaction, whereas the introduction of a hydrophilic group could rescue them. The tetrapeptide with stronger peptide-water interaction is also unable to form condensates and remains in a solution state even at a very high concentration. To rescue this type of tetrapeptide, increasing the peptide-peptide interaction by combining

two tetrapeptide molecules into one octapeptide through a disulfide bond could be a quite feasible method, which could dramatically increase the valence of each monomer peptide and decrease the minimal concentration needed for phase separation^{31,32}. Disulfide bonds formed due to oxidation of the thiol group (SH group) come from cysteine (C) residue, which is extensively present in many types of protein molecules, the formation and cleavage of disulfide bonds have been widely used by living systems to govern the basic biological process. Since disulfide bonds can be formed or broken by oxidation-reduction process by adding many kinds of oxidizing and reducing agents, we use hydrogen peroxide (H₂O₂) and dithiothreitol (DTT) to control phase separation process dynamically by controlling the formation and cleavage of disulfide bonds (Fig. 6a). The peptide YCGY has very good solubility in aqueous solution and can not undergo phase separation even at 80 mg/mL. However, it can undergo phase separation at a low concentration of 6 mg/mL through the formation of disulfide bonds by oxidation of the thiol group. The emulsion turns into a clear solution again after adding DTT (Fig. 6b). Besides the redox reaction, we can also control the phase separation by phosphorylation of peptides (Fig. S25). Moreover, the transformation between multiphasic and homogeneous condensates can also be controlled by disulfide bonds (Fig. 6c, 6d). The peptide WCRY forms homogeneous condensates, which transform into multiphasic condensates after oxidation by H₂O₂. The parallel group YCRY and WCGY show similar results with YCGY and WCRY (Figs. S26, S27), both peptides YCGY and YCRY form homogeneous droplets, WCGY and WCRY form core-shell droplets after the oxidation by H₂O₂, further demonstrating the increasing homotypical π - π interactions after molecules cross-linking are necessary for multiphasic condensates. Interestingly, the homogeneously distributed guest fluorescent molecules SBD were recruited into the newly formed inner core, which is similar to the cellular multiphasic condensates to recruit different biomacromolecules into different layers for fulfilling a variety of functions. In addition, the experiments with other fluorescent molecules, such as ThT, fluorescein, show similar results with SBD (Figure S27).

Discussion

In summary, this work describes symmetrical core-shell structural condensates formed through phase separation by chemical programming. The single component of tetrapeptide can synchronously assemble into a spherical core-shell structure under the external stimuli of pH or temperature. Hydrophobic interaction, π - π stacking, and hydrogen bonds synergistically contribute to condensate formation. The hydrophilic group in the aromatic ring is essential for the formation of condensates, given that its removal often leads to the aggregation of peptides. Moreover, the results suggested that the amino acid W is critical for forming a core-shell structure due to its strongest interaction strength compared with other amino acids. By encoding the amino acid composition of the tetrapeptides, we can design and synthesize not only homogeneous condensates but also condensates with core-shell structures. Finally, we show the transformation of homogeneous condensates to condensates with a core-shell structure under external stimuli. The transformation of structural organization within condensates results in the recruitment of homogeneously distributed guest molecules into the inner core, which allows us to control the distribution of guest molecules spatiotemporally. This work facilitates the rational design of synthetic core-shell condensates with various applications on demand and opens a door for synthesizing multiphasic condensates with a single component.

Methods

Material sources

Fmoc-amino acids, HBTU (O-(Benzotriazol-1-yl)-N, N, N', N'-tetramethyluronium hexafluorophosphate) and Rink Amide resin were obtained from GL Biochem (Shanghai, China). Rhodamine B,

Rhodamine 6 G, trifluoroacetic acid (TFA), triethylamine (TEA), N, N-diisopropylethylamine (DIPEA), NaOH, and triisopropylsilane (TIPS) were purchased from Aladdin (Shanghai, China). Coumarin 6 and fluorescein were purchased from Macklin (Shanghai, China). N, N'-dimethyl formamide (DMF) was obtained from J&K Scientific (Beijing, China). All other reagents were purchased from commercial sources and used without further purification.

Peptide synthesis

All peptides were synthesized by Fmoc-based solid-phase peptide synthesis (SPPS) (Fig. S1). Briefly, after the rink amide resin was swelling in DMF for 15 min, 20% piperidine was used to remove the Fmoc group, the first amino acid with side-chain protected in DMF was loaded to the resin by coupling reagent HBTU and DIPEA for 2 h. After washing 5 times by DMF, we used a deprotection agent (20% piperidine in DMF) to remove the Fmoc group. Then the growth of peptide chain follows the established Fmoc SPPS protocol. The product of the peptide was cleaved from the resin by using a cleavage reagent (TFA: TIPS: H₂O = 95%: 2.5%: 2.5) for 2 h. After the solvent was removed through rotary evaporation, ice-cold diethyl ether was added to the above residue. The resulting precipitate was centrifuged at 5000 g for 3 min at 4 °C. The supernatant was removed, the resulting crude peptide was further purified by High Performance Liquid Chromatography (HPLC).

The preparation of peptide condensate

The lyophilized tetrapeptide powder was dissolved in Milli-Q water with an adjusted pH of 7.5 by adding 0.5 M NaOH (aq.). The resulting milky emulsion was heated at 60 °C for 5 min and cooled to room temperature. Then the milky emulsion was detected by bright-field microscopy (Leica STELLARIS 8 FALCON confocal microscope). The final concentration (Table S1) of tetrapeptides is determined by their hydrophobicity and aromatic properties.

Turbidity measurement

We measured the turbidity of all the peptide solutions by spectrophotometer at the wavelength of 600 nm. All the measurements were carried out for three independent times at room temperature. The 0.1 M, 0.5 M, and 1.0 M NaOH were chosen depending on the concentration of different peptides and the added volume did not exceed 10% of the original volume. The same volume of Milli-Q water was used as the control group. The pH-dependent turbidity measurements were performed on a Microplate reader (Thermo Scientific Varioskan LUX). Other turbidities were measured by Agilent carry3500. The pH was measured by a pH meter (METTLER TOLEDO FE28 -Micro).

pH-concentration phase diagrams

The pH-concentration phase diagrams were measured in the following steps: we set 6 different concentrations for each peptide. For each specific concentration, 160 μ L peptide solution was prepared, then gradually increase the pH by adding NaOH (aq.) to the peptide solution and monitor the turbidity changes by spectrophotometer at the wavelength of 600 nm (Agilent carry3500). When turbidity (OD > 0.1) appears, measure the pH of the emulsion with a pH-meter (METTLER TOLEDO FE28 -Micro).

Fourier transform infrared spectroscopy of peptide condensates or the solution

The lyophilized tetrapeptide powder was dissolved in deuterium oxide (D₂O). The pH of the stock solution was adjusted to 7.5 by 0.5 M sodium deuteroxide (NaOD). Using a pipette to drop the solution or condensates of the peptide on a diamond single reflection attenuated total reflectance (ATR) module and examine their spectra by the FTIR micro spectrometer (ThermoFisher Nicolet iS50) with averaging 16 scans, spectral resolution of 4 cm⁻¹.

Raman spectroscopy of peptide solution and the condensates

10 μL of the samples were settled on the glass slide with a precoated sigmacote. For the peptide solution, average Raman spectra were obtained by VIS-NIR Confocal Raman Microscope System (WITec alpha 300 R). For the peptide condensates, we used a 50 \times magnification objective lens to focus the condensates at the bottom layer. Then we obtained their Raman spectra by using a 532 nm laser excitation with 10 mW laser power with a 10 s integration time and 10 times accumulation. For each sample, 5 different condensates were measured for statistical analysis.

Encapsulation efficiency of guests by condensates

After the formation of condensates, 1 μL fluorophore with a final concentration of 10 μM was added to 100 μL condensates emulsion, and the mixture was incubated for 1 h at rt., then the samples were centrifuged at 3000 $\times g$ for 20 min, then 20 μL of supernatant was diluted to 100 μL . Rhodamine 6 G and Rhodamine B were dissolved in water. Coumarin 6, Resorufin Sodium Salt, SBD, and Red BODIPY were dissolved in DMSO. The concentration of the fluorophores in the supernatant was measured via fluorescence. The efficiency of encapsulation (%EE) was calculated using $\%EE = C_{Total} - C_{supernatant} / C_{Total}$. We tested the encapsulation of WYWW at pH 9.0 because the condensates formed by WYWW tend to aggregate at pH 7.5 when the fluorophores were added but are relatively stable at pH 9.0.

Fluorescence recovery after photobleaching (FRAP)

After the formation of condensates, 0.1 μL solution of fluorescein (1 mM, DMSO) was added to the solution. About 10 μL emulsion was settled on the glass slide with precoated sigmacote and left for 16 h before the FRAP experiment to allow the small condensates to fuse into the big one. The photobleach and fluorescence recovery processes were recorded by a Leica STELLARIS 5 FALCON confocal microscope at the excitation wavelength of 488 nm. $I_{norm}(t) = I_{frap}(t) / A \cdot I_{ref}(t)$. The $I_{frap}(t)$, the intensity of the bleached region is scaled $I_{ref}(t)$, the intensity of the droplet before photo-bleached, where $A = I_{frap}(t < t_{frap}) / I_{ref}(t < t_{ref})$ is the mean scaled intensity before bleaching.

Fast fluorescence lifetime imaging microscopy (FLIM) of condensates

A drop of phase-separated solutions was settled on the glass coverslip for imaging. The FLIM images were acquired by a Leica STELLARIS 8 FALCON confocal microscope equipped with a pulsed white laser (WLL) using an X63/1.40 oil immersion objective. The SBD was excited by a 448 nm laser line with a frequency of 10 MHz, respectively. The fluorescent lifetime fitting and image analysis were performed in LAS X and Fiji.

Samples preparation for Cryo-EM, Cryo-SEM, Cryo-FIB

About 3 μL emulsion were applied onto glow-discharged holey carbon grids (Quantifoil Cu RL2/L3, 300 mesh), blotted with a Vitrobot Marker IV (Thermo Fisher Scientific) for 3 s under 100% humidity at 4 $^{\circ}\text{C}$, and subjected to plunge freezing into liquid ethane.

Cryo-FIB milling

Vitrified samples were further processed by cryo-FIB milling. A dual-beam microscope FIB/SEM Aquilos 2 (Thermo Fisher Scientific) equipped with a cryo-transfer system (Thermo Fisher Scientific) and rotatable cryo-stage cooled at -191°C by an open nitrogen circuit was used to carry out the thinning. Prior to the milling, the grids were mounted on the shuttle and transferred onto the cryo-stage, followed by the coating with an organometallic Platinum layer using the GIS system (Thermo Fisher Scientific) for 5–6 s. Then, condensates positioned approximately in the centers of grid squares were selected for thinning. Thinning was carried out under the condition of voltage 30 kV and current 10 pA until the material around the ball was burned off.

Redox-reaction-controlled condensate formation

The lyophilized tetrapeptide powder YCGY was dissolved in Milli-Q water, then the pH of the resulting homogeneous solution (200 mL, 10 mg/mL) was adjusted to 7.5 by using 0.5 M NaOH. Then 5 μL was taken out and examined by CLSM. Then 2 μL H_2O_2 (1 M) was added to the remaining residual solution. After incubating at room temperature for 5 mins, 5 μL of the solution was taken out for observation by CLSM. Then 2.5 DTT (1 M) was added to the residual liquid and incubated for 5 mins at room temperature before observing by CLSM.

Redox controlled the condensate transformation between homogeneous and core-shell structures

The lyophilized tetrapeptide powder WCRY was dissolved in Milli-Q water and the pH was adjusted to 7.5 using 1 M NaOH. After the condensate formation, 0.1 μL SBD (1 mM, DMSO) was added to 100 μL (30 mg/mL) condensate emulsion and incubated at room temperature for 5 mins. Then 5 μL was taken out for the observation by CLSM and fast FLIM imaging. Then 1 μL H_2O_2 (1 M) was added to the remaining residual solution and incubated at room temperature for 5 mins before confocal and fast FLIM imaging.

Multiscale molecular dynamics simulations

Construct fiber-like structures as the core of tetrapeptide condensates. To construct the ordered core of the tetrapeptide systems, we utilized the Cryo-EM structure of the I-KMe₃ fiber (PDB ID: 6X5I)⁵⁷, a structure formed by short peptides. Using this as a reference structure, we retained only the backbone atoms of the first four amino acids in each peptide and removed the remaining atoms. We then used the Scwrl4⁶¹ software to add side chain atoms corresponding to the representative tetrapeptide sequences studied experimentally: WRWW, GWWW, YRYY, and YGY. To facilitate subsequent simulations, as detailed in the *Supporting Information*, we rotated each layer of the fiber to align properly and satisfy the periodic boundary conditions. The resulting fiber-like core structure contains a total of 70 monomers.

MARTINI simulations. The multiscale simulations began with MARTINI simulations. For each tetrapeptide sequence, the monomer and the core configurations were converted to MARTINI representations using martinize2⁶². The MARTINI structure of the core was placed at the center of a 4.9 nm \times 8.0 nm \times 20 nm simulation box, and 130 peptides were randomly inserted, resulting in a total of 200 peptides. The box was then solvated with MARTINI water and 100 mM NaCl was added. Following energy minimization and equilibration, we conducted an NPT (Constant temperature, constant pressure) simulation at 303.15 K and 1 bar for 1 microsecond. Positional restraints were applied to the backbone beads of the core to maintain its position. The MARTINI 3 force field⁶³ was used for these simulations.

Tetrapeptides including WRWW, GWWW, YRYY, and YGY were simulated following this protocol. For each sequence, two simulations were conducted for either acidic or basic conditions, with the only difference being whether the N-termini of peptides were protonated, resulting in a total of eight simulations. Additionally, a core-only system for WRWW in a basic environment was constructed, mirroring the setup of the previous systems but without the insertion of 130 peptide monomers. Further details can be found in the *Supporting Information*.

Atomistic simulations. The last frame of the MARTINI simulation was converted to an atomistic configuration using the backward script⁶³, serving as the initial configuration for atomistic simulations. After energy minimization, a 120 ns equilibration simulation was conducted, during which positional restraints on the core structure gradually removed. The production simulation was then run in the NPT ensemble for 750 ns at 303.15 K and 1 bar, using the CHARMM36m⁵⁹ force field with the modified TIP3P water model⁶⁴. Additional details are available in the *Supporting Information*.

Simulation analysis. The all-atom simulations were analyzed to determine the average atom density profiles. For a given simulation trajectory and time window, the average atom density across the *yz* plane of the simulation box, which is orthogonal to the fiber-like core, was calculated and averaged over all frames in the time window. The densities of core peptides, shell peptides, and water molecules were quantified separately. Detailed analysis methods are provided in the *Supporting Information*.

Multiscale molecular dynamics simulations for beta-strands

The initial beta-strand structures, each containing 5 peptides, were extracted from the fiber-like core structure used in the core-shell simulations. To set up the simulation box, 14 replicas of the β -strand structures were placed in a 4.9 nm \times 8.0 nm \times 20 nm box, along with 130 free peptides, resulting in a total of 200 peptides. The box was then solvated with water, and 100 mM NaCl was added. The multiscale MD simulations followed the protocols previously described for the core-shell systems, with the exception that the all-atom simulations were conducted for 250 ns. Separate simulations were performed for WRWW and YRYY under basic conditions.

Statistics and reproducibility

For all representative Cryo-EM, Cryo-FIB-SEM, TEM, Bright-field, CLSM, Fast FLIM and optical images, experiments were performed three times independently with similar results.

Reporting summary

Further information on research design is available in the Nature Portfolio Reporting Summary linked to this article.

Data availability

All the data that support the findings are available within the main text, Supplementary Information and from corresponding author(s) upon request. Simulation trajectories used for analysis are available at <https://doi.org/10.5281/zenodo.14877253>. Source data are provided with this paper.

Code availability

The code used for constructing the initial ordered core structure and analyzing simulation trajectories is available at <https://doi.org/10.5281/zenodo.14877253>.

References

- Hyman, A. A., Weber, C. A. & Jülicher, F. Liquid-liquid phase separation in biology. *Annu. Rev. Cell Dev. Biol.* **30**, 39–58 (2014).
- Shin, Y., Brangwynne, C. P. Liquid phase condensation in cell physiology and disease. *Science* **357**, (2017).
- Banani, S. F. et al. Biomolecular condensates: organizers of cellular biochemistry. *Nat. Rev. Mol. Cell Biol.* **18**, 285–298 (2017).
- Jain, S. et al. ATPase-Modulated Stress Granules Contain a Diverse Proteome and Substructure. *Cell* **164**, 487–498 (2016).
- Feric, M. et al. Coexisting Liquid Phases Underlie Nucleolar Subcompartments. *Cell* **165**, 1686–1697 (2016).
- Lafontaine, D. L. J. et al. The nucleolus as a multiphase liquid condensate. *Nat. Rev. Mol. Cell Biol.* **22**, 165–182 (2021).
- Latham, A. P., Zhang, B. Molecular Determinants for the Layering and Coarsening of Biological Condensates. *Aggregate (Hoboken)* **3**, (2022).
- Alberti, S. & Hyman, A. A. Biomolecular condensates at the nexus of cellular stress, protein aggregation disease and ageing. *Nat. Rev. Mol. Cell Biol.* **22**, 196–213 (2021).
- Holehouse, A. S. & Pappu, R. V. Functional Implications of Intracellular Phase Transitions. *Biochemistry* **57**, 2415–2423 (2018).
- Gabryelczyk, B. et al. Hydrogen bond guidance and aromatic stacking drive liquid-liquid phase separation of intrinsically disordered histidine-rich peptides. *Nat. Commun.* **10**, 5465 (2019).
- Wang, J. et al. A Molecular Grammar Governing the Driving Forces for Phase Separation of Prion-like RNA Binding Proteins. *Cell* **174**, 688–699.e616 (2018).
- Abbas, M. et al. Peptide-based coacervates as biomimetic protocells. *Chem. Soc. Rev.* **50**, 3690–3705 (2021).
- Kilgore, H. R. & Young, R. A. Learning the chemical grammar of biomolecular condensates. *Nat. Chem. Biol.* **18**, 1298–1306 (2022).
- Aumiller, W. M. Jr. & Keating, C. D. Phosphorylation-mediated RNA/peptide complex coacervation as a model for intracellular liquid organelles. *Nat. Chem.* **8**, 129–137 (2016).
- Simon, J. R. et al. Programming molecular self-assembly of intrinsically disordered proteins containing sequences of low complexity. *Nat. Chem.* **9**, 509–515 (2017).
- Abbas, M. et al. A short peptide synthon for liquid-liquid phase separation. *Nat. Chem.* **13**, 1046–1054 (2021).
- Sun, Y. et al. Phase-separating peptides for direct cytosolic delivery and redox-activated release of macromolecular therapeutics. *Nat. Chem.* **14**, 274–283 (2022).
- Baruch Leshem, A. et al. Biomolecular condensates formed by designer minimalistic peptides. *Nat. Commun.* **14**, 421 (2023).
- Kubota, R., Torigoe, S. & Hamachi, I. Temporal Stimulus Patterns Drive Differentiation of a Synthetic Dipeptide-Based Coacervate. *J. Am. Chem. Soc.* **144**, 15155–15164 (2022).
- Feng, Z., Wang, H. & Xu, B. Instructed assembly of peptides for intracellular enzyme sequestration. *J. Am. Chem. Soc.* **140**, 16433–16437 (2018).
- Jain, A. et al. Connected peptide modules enable controlled coexistence of self-assembled fibers inside liquid condensates. *J. Am. Chem. Soc.* **144**, 15002–15007 (2022).
- Kaur, T. et al. Sequence-encoded and composition-dependent protein-RNA interactions control multiphase condensate morphologies. *Nat. Commun.* **12**, 872 (2021).
- Choi, S. et al. Phase-specific RNA accumulation and duplex thermodynamics in multiphase coacervate models for membraneless organelles. *Nat. Chem.* **14**, 1110–1117 (2022).
- Lu, T. & Spruijt, E. Multiphase Complex Coacervate Droplets. *J. Am. Chem. Soc.* **142**, 2905–2914 (2020).
- Ye, S. et al. Micropolarity governs the structural organization of biomolecular condensates. *Nat. Chem. Biol.* **20**, 443–451 (2024).
- Abyzov, A., Blackledge, M. & Zweckstetter, M. Conformational Dynamics of Intrinsically Disordered Proteins Regulate Biomolecular Condensate Chemistry. *Chem. Rev.* **122**, 6719–6748 (2022).
- Bremer, A. et al. Deciphering how naturally occurring sequence features impact the phase behaviours of disordered prion-like domains. *Nat. Chem.* **14**, 196–207 (2022).
- Martin, E. W. et al. Valence and patterning of aromatic residues determine the phase behavior of prion-like domains. *Science* **367**, 694–699 (2020).
- Brangwynne, C. P., Tompa, P. & Pappu, R. V. Polymer physics of intracellular phase transitions. *Nat. Phys.* **11**, 899–904 (2015).
- Alberti, S. et al. A systematic survey identifies prions and illuminates sequence features of prionogenic proteins. *Cell* **137**, 146–158 (2009).
- Ribeiro, S. S. et al. The synergic effect of water and biomolecules in intracellular phase separation. *Nat. Rev. Chem.* **3**, 552–561 (2019).
- Pappu, R. V. et al. Phase Transitions of Associative Biomacromolecules. *Chem. Rev.* **123**, 8945–8987 (2023).
- Dougherty, D. A. Cation- π interactions in chemistry and biology: a new view of benzene, Phe, Tyr, and Trp. *Science* **271**, 163–168 (1996).

34. Scheiner, S., Kar, T. & Pattanayak, J. Comparison of various types of hydrogen bonds involving aromatic amino acids. *J. Am. Chem. Soc.* **124**, 13257–13264 (2002).
35. Li, Q. et al. LLPSSDB: a database of proteins undergoing liquid–liquid phase separation in vitro. *Nucleic Acids Res* **48**, D320–D327 (2019).
36. Schlamadinger, D. E., Gable, J. E. & Kim, J. E. Hydrogen bonding and solvent polarity markers in the uv resonance raman spectrum of tryptophan: application to membrane proteins. *J. Phys. Chem. B* **113**, 14769–14778 (2009).
37. Takeuchi, H. Raman structural markers of tryptophan and histidine side chains in proteins. *Biopolymers* **72**, 305–317 (2003).
38. Schlamadinger, D. E. et al. UV resonance Raman study of cation- π interactions in an indole crown ether. *J. Raman Spectrosc.* **42**, 633–638 (2011).
39. Ryan, D. M. et al. Effect of C-terminal modification on the self-assembly and hydrogelation of fluorinated Fmoc-Phe derivatives. *Langmuir* **27**, 4029–4039 (2011).
40. Alberti, S., Gladfelter, A. & Mittag, T. Considerations and Challenges in Studying Liquid-Liquid Phase Separation and Biomolecular Condensates. *Cell* **176**, 419–434 (2019).
41. Seo, J. et al. An infrared spectroscopy approach to follow β -sheet formation in peptide amyloid assemblies. *Nat. Chem.* **9**, 39–44 (2017).
42. Barth, A. Infrared spectroscopy of proteins. *Biochim. Biophys. Acta* **1767**, 1073–1101 (2007).
43. Lampel, A. et al. Polymeric peptide pigments with sequence-encoded properties. *Science* **356**, 1064–1068 (2017).
44. Pavia, D. L. et al. Chapter 2 -Infrared Spectroscopy. *Introduction to Spectroscopy (Fifth Edition)*, 2013.
45. Colthup, N. B., Daly, L. H., Wiberley, S. E. Chapter 2 - Ir Experimental Considerations. *Introduction to Infrared and Raman Spectroscopy (Third Edition)*, 1990.
46. Siamwiza, M. N. et al. Interpretation of the doublet at 850 and 830 cm^{-1} in the Raman spectra of tyrosyl residues in proteins and certain model compounds. *Biochemistry* **14**, 4870–4876 (1975).
47. Hernández, B. et al. All characteristic Raman markers of tyrosine and tyrosinate originate from phenol ring fundamental vibrations. *J. Raman Spectrosc.* **47**, 210–220 (2016).
48. Infield, D. T. et al. Cation- π Interactions and their Functional Roles in Membrane Proteins. *J. Mol. Biol.* **433**, 167035 (2021).
49. Shao, J. et al. The Role of Tryptophan in π Interactions in Proteins: An Experimental Approach. *J. Am. Chem. Soc.* **144**, 13815–13822 (2022).
50. Cao, S. et al. Dipeptide coacervates as artificial membraneless organelles for bioorthogonal catalysis. *Nat. Commun.* **15**, 39 (2024).
51. Marguet, M., Bonduelle, C. & Lecommandoux, S. Multi-compartmentalized polymeric systems: towards biomimetic cellular structure and function. *Chem. Soc. Rev.* **42**, 512–529 (2013).
52. Mu, W. et al. Superstructural ordering in self-sorting coacervate-based protocell networks. *Nat. Chem.* **16**, 158–167 (2024).
53. Zhou, X. et al. Mutations linked to neurological disease enhance self-association of low-complexity protein sequences. *Science* **377**, eabn5582 (2022).
54. Wadsworth, G. M. et al. RNAs undergo phase transitions with lower critical solution temperatures. *Nat. Chem.* **15**, 1693–1704 (2023).
55. Xu, T. et al. Accelerating the prediction and discovery of peptide hydrogels with human-in-the-loop. *Nat. Commun.* **14**, 3880 (2023).
56. Li, J. et al. Aromatic-Aromatic Interactions Enable α -Helix to β -Sheet Transition of Peptides to Form Supramolecular Hydrogels. *J. Am. Chem. Soc.* **139**, 71–74 (2017).
57. Feng, Z. et al. Artificial Intracellular Filaments. *Cell Rep. Phys. Sci.* **1**, 100085 (2020).
58. Souza, P. C. T. et al. Martini 3: a general purpose force field for coarse-grained molecular dynamics. *Nat. Methods* **18**, 382–388 (2021).
59. Huang, J. et al. CHARMM36m: an improved force field for folded and intrinsically disordered proteins. *Nat. Methods* **14**, 71–73 (2017).
60. Ester, M. et al. A density-based algorithm for discovering clusters in large spatial databases with noise. *Proceedings of the Second International Conference on Knowledge Discovery and Data Mining*. Portland, Oregon: AAAI Press. pp. 226–231; (1996)
61. Krivov, G. G., Shapovalov, M. V. & Dunbrack, R. L. Jr. Improved prediction of protein side-chain conformations with SCWRL4. *Proteins: Struct., Funct., Bioinforma.* **77**, 778–795 (2009).
62. Kroon, P. C. et al. Martinize2 and Vermouth: Unified Framework for Topology Generation. eLife Sciences Publications, Ltd; (2024).
63. Wassenaar, T. A. et al. Going Backward: A Flexible Geometric Approach to Reverse Transformation from Coarse Grained to Atomistic Models. *J. Chem. Theory Comput.* **10**, 676–690 (2014).
64. MacKerell, A. D. et al. All-atom empirical potential for molecular modeling and dynamics studies of proteins. *J. Phys. Chem. B* **102**, 3586–3616 (1998).

Acknowledgements

This project was supported by the National Natural Science Foundation of China (82272145, to H.W.) and the Foundation of Westlake University. We thank the Instrumentation and Service Center for Molecular Sciences, Instrumentation and Service Center for Physical Sciences, General Equipment Core Facility, Biomedical Research Core Facilities, and Laboratory Animal Resource Center at Westlake University for the assistance with measurements. We acknowledge Xiaojuan Wang for help with the Cryo-FIB experiments and Zhong Chen for help with the Raman experiments. We thank Liheng Lu for help with synthesizing part of peptides and Jianan Dai for help with synthesizing part of fluorophores.

Author contributions

H.M.W. conceptually designed the strategy for this study, provided intellectual input, supervised the studies, and revised the manuscript. Lai.C. Z. designed the study and performed most of the experiments. Long.C. Z. and X. Z. performed the FLIM experiments. C.W. and B. Z. did MD simulations. T.Y.X., J.W. synthesized some peptides and performed CLSM experiments. H.M.W. and Lai. C.Z. wrote the manuscript with contributions from all authors.

Competing interests

The authors declare no competing interests

Additional information

Supplementary information The online version contains supplementary material available at <https://doi.org/10.1038/s41467-025-58060-6>.

Correspondence and requests for materials should be addressed to Bin Zhang, Xin Zhang or Huaimin Wang.

Peer review information *Nature Communications* thanks Vincenzo Carnevale and the other, anonymous, reviewer(s) for their contribution to the peer review of this work. A peer review file is available.

Reprints and permissions information is available at <http://www.nature.com/reprints>

Publisher's note Springer Nature remains neutral with regard to jurisdictional claims in published maps and institutional affiliations.

Open Access This article is licensed under a Creative Commons Attribution-NonCommercial-NoDerivatives 4.0 International License, which permits any non-commercial use, sharing, distribution and reproduction in any medium or format, as long as you give appropriate credit to the original author(s) and the source, provide a link to the Creative Commons licence, and indicate if you modified the licensed material. You do not have permission under this licence to share adapted material derived from this article or parts of it. The images or other third party material in this article are included in the article's Creative Commons licence, unless indicated otherwise in a credit line to the material. If material is not included in the article's Creative Commons licence and your intended use is not permitted by statutory regulation or exceeds the permitted use, you will need to obtain permission directly from the copyright holder. To view a copy of this licence, visit <http://creativecommons.org/licenses/by-nc-nd/4.0/>.

© The Author(s) 2025